Clays and Clay Minerals, Vol. 60, No. 5, 484–495, 2012.

THE CHARACTERIZATION OF $CaCO_3$ IN A GEOTHERMAL ENVIRONMENT: A SEM/TEM-EELS STUDY

JIN-WOOK KIM[1,]*, TOSHIHIRO KOGURE[2], KIHO YANG[1], SANG-TAE KIM[3], YOUNG-NAM JANG[4],
HION-SUCK BAIK[5], AND GILL GEESEY[6]

[1] Department of Earth System Sciences, Yonsei University, 134 Shinchon-dong, Seodaemoon-gu, Seoul, 120-749, Korea
[2] Department of Earth and Planetary Science, Graduate School of Science, The University of Tokyo,
7-3-1 Hongo, Bunkyo-ku, Tokyo, 113-0033, Japan
[3] School of Geography and Earth Sciences, McMaster University, 1280 Main Street West, Hamilton, ON, Canada L8S 4K1
[4] Korea Institute of Geoscience and Mineral Resources, Daejeon, 305-350, Korea
[5] Korea Basic Science Institute, 126-16, Anam-dong, Seongbuk-gu, Seoul, 136-713, Korea
[6] Department of Microbiology, Montana State University, Bozeman, Montana 59717-3210, USA

Abstract—Mineralization of microbial biomass is a common phenomenon in geothermal habitats, but knowledge of the structure of the minerals formed in these environments is limited. A combination of spectroscopic, microscopic, and stable isotopic methods, as well as the chemical analysis of spring water, were employed in the present study to characterize calcium carbonate minerals deposited in filamentous cyanobacterial mats in different locations of La Duke hot spring, a circumneutral thermal feature near the north entrance of Yellowstone National Park, Montana, USA. Calcite was the primary crystalline mineral phase associated with biofilm-containing deposits closest to the source of the spring and the suspended microbial biomass in a pool further from the source. The carbonate minerals at all sites occurred as aggregated granules, ~2 μm in diameter, in close association with the microbial biomass. Only in the deposits closest to the source were the granules organized as laminated structures interspersed with microbial biomass. The calcium carbonate grains contained two distinct regions: a dense monolithic calcite core and a porous dendritic periphery containing organic matter (OM). Electron energy loss spectroscopy (EELS) indicated that the voids were infilled with OM and carbonates. The EELS technique was employed to distinguish the source of carbon in the organic matter and carbonate mixture. The studies of carbon isotope compositions of the calcium carbonates and the saturation indices for calcite in the spring waters suggest that processes (abiotic *vs*. biotic) controlling the carbonate formation may vary among the sampling sites.

Key Words—Calcium Carbonate Precipitate, Carbon Isotope, Cyanobacterial Mat, Electron Energy Loss Spectroscopy, Focused Ion Beam, Transmission Electron Microscopy.

INTRODUCTION

The formation of calcium carbonate deposits has been shown to be influenced by both biotic and abiotic processes. Aerobic phototrophic cyanobacteria are thought to promote the precipitation of calcium carbonate deposits in various freshwater systems (Thompson and Ferris, 1990; Robbins and Yates, 1998; Knorre and Krumein, 2000). Cyanobacteria of the genus *Synechococcus* have been shown to promote the precipitation of calcium carbonate under oligotrophic, carbonate-rich conditions (Pentecost and Riding, 1986; Weisse *et al.*, 1993; Merz-Preiß, 2000; Merz-Preiß and Riding, 1999). These organisms influence the alkalinity of the water through the uptake of dissolved inorganic carbon (DIC) as part of photosynthesis during the day (light) and the release of carbon dioxide as a result of respiration during the night (dark) (Pentecost, 1985, 2003; Castanier *et al.*, 1999; Arp *et al.*, 2001; Dittrich *et al.*, 2003; Shiraishi *et al.*, 2008; Kandianis *et al.*, 2008). Abiotic processes that lead to the formation of calcium carbonate deposits include the spontaneous precipitation of salt as a result of its supersaturation in the bulk water with respect to calcite or aragonite through the degassing of CO_2 from solution (Ford and Pedley, 1996; Jacobson and Usdowski, 1975). The relative importance of biotic and abiotic reactions in the calcification and carbonate-precipitation reactions is probably influenced by a number of factors including the abundance, activity, and type of cyanobacteria in the system as well as pH, the total concentration of DIC, and Ca^{2+} (Arp, 2001; Dittrich *et al.*, 2003). In thermal environments, the water chemistry, hydrologic transport, climate, and bacterial community influenced the formation and depositional facies of travertine (Fouke *et al.*, 2000, 2003).

The structure of a calcium carbonate mineral in a natural environment (*i.e.* microbial mat in this study) may contain an important clue about its mineralogical genesis; however, understanding the mineralization of

---

* E-mail address of corresponding author:
jinwook@yonsei.ac.kr
DOI: 10.1346/CCMN.2012.0600505

calcium carbonate in a natural environment remains a topic of debate. The extracellular polymeric substances (EPS) excreted by the organisms are believed to limit the diffusion of metabolites, such as HCO_3^- and $CO_{2(aq)}$, leading to the formation of alkalinity gradients (Merz-Preiß, 2000). In addition, the negatively charged residues of the EPS of many cyanobacteria sequester the positively charged calcium ions from the bulk aqueous phase and serve as nucleation sites for calcium carbonate precipitation (Schultze-Lam *et al.*, 1996; Pratt, 2001; Fouke *et al.*, 2000; Bosak and Newman, 2003; Aloisi *et al.*, 2006; Aloisi, 2008; Obst *et al.*, 2009a, 2009b). Three-dimensional chemical mapping has revealed a spatial relationship between the EPS organic carbon and calcium distribution in a microbial nucleation model (Obst *et al.*, 2009b). The formation of calcium carbonate deposits around cyanobacterial biomass has also been observed in advection-dominated transport regimes (Kandianis *et al.*, 2008). Other cyanobacterial structures have also been shown to serve as nucleation sites for calcium carbonate precipitation under laboratory conditions. Transmission electron microscopy (TEM) revealed (Aloisi *et al.*, 2006) that nanoglobules excreted by cells were the nucleation sites for the precipitation reaction but subsequent crystal growth was not investigated. The precipitation of aragonite-like amorphous calcium carbonate (ACC) on cyanobacterial cell surfaces was suggested by Obst *et al.* (2009a) to be a transient precursor phase of calcite formation.

In the present investigation, calcium carbonates associated with cyanobacterial mats at different locations in a hot spring exhibited different morphologies and structures and thus offered insight into the mechanisms of carbonate precipitation in the mat environment. Systematic microscopic analysis of the calcium carbonates in La Duke hot spring has not been done before. Focused ion beam (FIB) sample-preparation technique for TEM-EELS observation was utilized to investigate a cross-section of a carbonate grain for nanoscale structural and chemical information which provides insight into the mechanism of carbonate formation.

MATERIALS AND METHODS

Site description

La Duke hot spring is a circumneutral geothermal feature on the shoulder of US Highway 89, ~5 miles north of Gardiner, Montana (45.1ºN 110.8ºW). Hot water exits the ground from the side of the mountain, flows over a mound of precipitated calcium carbonate before entering a ditch where the water temporarily pools before draining into the Yellowstone River through a culvert under the highway. Layers of cyanobacteria forming a green and orange microbial mat on the water surface and solid layers of precipitations around the hot spring are noticeable (Figure 1). Where the mound forms the edge of the pool (L4), the precipitated calcium carbonate exists as layers separated by filamentous microbial biomass growing as a biofilm. In the pool, calcium carbonate is dispersed in masses of filamentous microbial biomass suspended in the water column (L1–L3) (Figure 1). The water temperature and pH values for L1, L2, L3, and L4 were measured at 62ºC (pH = 6.7), 62ºC (pH =6.7), 62ºC (pH = 6.7), and 65ºC (pH = 7.2), respectively, using a thermometer and pH paper.

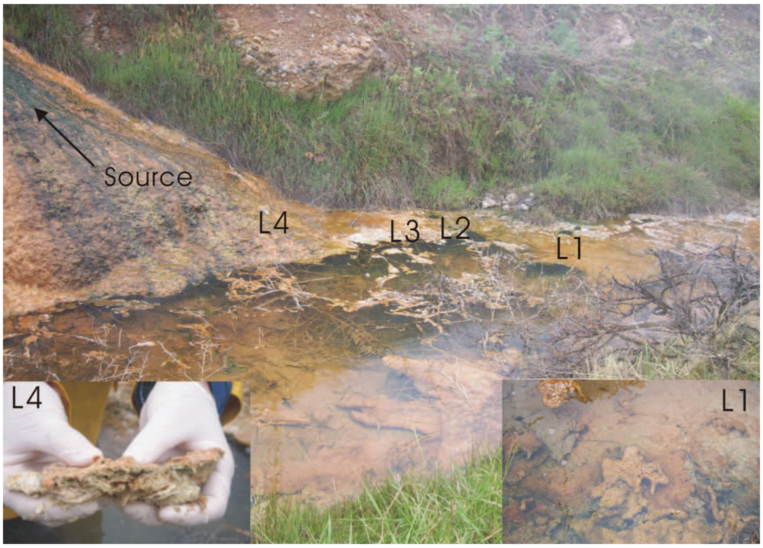

Figure 1. Sampling location in La Duke hot spring, Yellow Stone National Park, USA, containing a mound consisting of mineral layers interspersed with microbial mat (L4), which extended from the source of the spring to the pool of water that accumulated in the ditch (L1, L2, L3). The pool contained suspended microbial mat at the air–water interface.

Sample collection

The mixture of solid carbonate precipitates and gelatinous microbial mat was collected from areas L1, L2, and L3 of the ditch while a solid carbonate sample was collected from the steep edges of the mound where it intersects the ditch at area L4 (Figure 1). The samples were placed in Whirl-Pak bags, and stored on ice during transport to the laboratory where they were stored at −4ºC until analyzed.

Water was collected for stable-isotope analysis of dissolved inorganic carbon (DIC) where it surfaced from the ground following previously described protocols (Atekwana *et al.*, 2004). Briefly, an ammonium-$SrCl_2$ solution was prepared by dissolving 360 g of $SrCl_2 \cdot H_2O$ in 400 mL of 25% NH_4OH in a N_2-purged glove box to exclude atmospheric CO_2 from the solution. After aging for 3 days to precipitate any residual dissolved CO_2, 225 mL of the aqueous phase was transferred to N_2-purged 250-mL polyethylene bottles under a N_2 atmosphere. The bottles were capped, sealed with PVC tape, and transported to the sampling sites. 60-mL plastic syringes were filled with spring water and the water transferred to the bottom of each bottle using a 3.5 cm-long syringe needle, causing some of the ammonium-$SrCl_2$ solution to be displaced from the bottle and leaving no headspace in the bottle. Care was taken to avoid introduction of atmospheric CO_2 during filling of the syringe and bottle. Each bottle was resealed and shaken to promote precipitation of $SrCO_3$. After allowing the precipitated $SrCO_3$ to settle overnight, the bulk of the aqueous phase was decanted, the precipitate resuspended in the remaining aqueous phase and the suspension filtered through a Whatman #5 filter, all under a N_2 atmosphere. The precipitate trapped on the filter was dried overnight at 60ºC and stored in sealed plastic containers prior to isotope analysis.

Samples for water chemistry were also collected at each area (L1−L4). The samples were filtered through 0.45 μm cellulose membrane disc filters and then placed in 15-mL bottles. Subsequently, the filtered water samples for the cation analysis were treated with a 1:1 volume ratio of 0.5% hydrochloric acid and 1% nitric acid to maintain the cation species in the state of pH < 2.

X-ray diffraction and microscopy

A subsample of solids containing biomass and carbonate precipitates was thawed, dried, and then gently crushed using a mortar and pestle. The dried material was then analyzed by X-ray diffraction (XRD), using a Rigaku RINT-ultima diffractometer with CuKα radiation and a diffracted-beam, graphite monochromator, to identify the mineral phases. In order to determine the calcite/aragonite volume ratio, the theoretical intensity ratio between calcite 012 and aragonite 111 reflections was calculated (see Figure 2 for the potions of these reflections in XRD patterns) (Kogure, 2003). The integral intensity per unit volume for a reflection *hkl* in the powder diffraction pattern is proportional to

$$\frac{|F_{hkl}|^2}{V_c^2} \cdot LP(\theta) \cdot n$$

where F_{hkl}, V_c, $LP(\theta)$, and n are the structure factor for the reflection, unit-cell volume, Lorenz and polarization factor at the diffraction angle (θ), and multiplicity of the reflection, respectively. These values calculated for calcite 012 were 32.76 (the structure factor is given in units of multiples of the unit of scattering by a single electron, 2.82×10^{-15} M), 367.8 $Å^3$, 10.69 at $\theta = 11.54º$, and 6, whereas they were 41.94, 226.87 $Å^3$, 8.18 at $\theta = 13.13º$, and 8, respectively, for aragonite 111. Consequently the intensity ratio, $I_{111\text{-arago}}/I_{012\text{-cal}}$, from the specimen with the same volume of aragonite and calcite was 4.40. As the absorption coefficients of calcite and aragonite for CuKα were similar, the ratio between experimental $I_{111\text{-arago}}/I_{012\text{-cal}}$ and its theoretical value (4.40) corresponds to the volume ratio of the two phases in the specimen.

Another subsample of solids was thawed and washed in distilled water, air dried, and embedded in epoxy resin. After curing, the resin blocks were sliced,

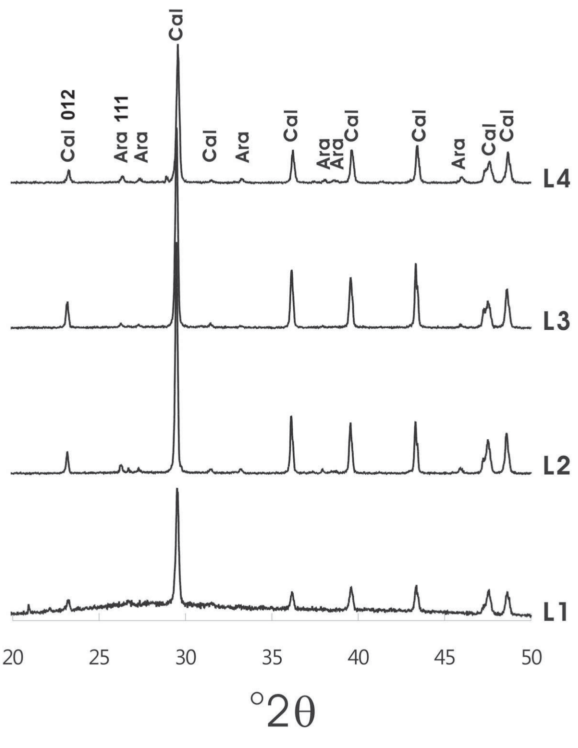

Figure 2. XRD patterns of samples from areas L1, L2, L3, and L4 showing calcite (Cal) as a major mineral component. Low-intensity aragonite (Ara) peaks were also detected except in L1, which was probably due to the peak noise associated with organic matter overlapping the aragonite peaks.

deposited on glass slides, and examined using optical microscopy (Olympus BX60 with a CCD camera, both plane polarized light and crossed polars). Plane-polarized optics provides information on mineral color, shape, and refractive index. Crossed-polars optics provides interference colors as the stage is rotated to aid in mineral identification. Another subsample of thawed solids was dried and coated with a 5 nm-thick Pt-Pd film and examined by scanning electron microscopy (SEM) using a Hitachi S-4500 SEM with a field-emission electron gun operated at 5 kV. Samples containing areas of interest based on SEM examination were prepared as ultrathin sections using a focused ion beam (FIB) system with a micro-sampling function (Hitachi FB-2100) as described previously (Kameda *et al.*, 2008) and examined by TEM, using a JEOL JEM-2010UHR instrument equipped with a JEOL JED-2200 EDS operating at an accelerating voltage of 200 kV. Samples were also subjected to EELS analysis using a TECNAI F30 ST TEM (FEI Company, Hillsboro, Oregon, USA) equipped with a Gatan imaging filter (GIF895) and operated at an accelerating voltage of 300 keV. The EELS spectra were collected at a convergence angle of 5 mrad, a collection angle of 2 mrad, a 2.0-mm entrance aperture, and energy dispersion of 0.5 eV/channel. L-edge spectra were acquired with an integration time between 2.0 and 5.0 s. Spectra were collected in diffraction mode (*i.e.* image coupling to the EELS spectrometer). The EELS quantification of elemental distribution was performed by means of a three-window method which uses two pre-edge windows to compute the background contribution to the post-edge (Kim and Dong, 2011). The relative proportions of elements were calculated based on the peak intensity followed by the subtraction of the computed background component by power-law extrapolation (statistical prediction model) using Digital Micrograph software. The spectra were corrected for dark current and channel-to-channel gain variation of the charge-coupled device (CCD) detector.

Stable isotope analysis

Dissolved inorganic carbon (DIC) in the hot spring water was quasi-instantaneously and quantitatively precipitated as $SrCO_3$ by mixing ammonium-$SrCl_2$ solution with the spring water. Subsequently, the carbon isotope composition of the DIC of the spring water was determined by analyzing the $\delta^{13}C$ value of the $SrCO_3$. The carbon isotope compositions of the $CaCO_3$ as well as the $SrCO_3$ samples were determined using the classical method of McCrea (1950). All carbonate samples were analyzed at 90ºC on a VG-OPTIMA isotope ratio mass spectrometer (IRMS) equipped with an automated IsoCarb system at McMaster University. Two international standards, NBS-18 ($\delta^{13}C = -5.04‰$) and NBS-19 ($\delta^{13}C = +1.95‰$), were analyzed with the carbonate samples in order to normalize the carbon isotope compositions of the sample carbonates. The overall analytical precision (1σ) of the $\delta^{13}C$ measurements on these two standards was better than ±0.04‰ and the carbon isotope compositions are reported relative to V-PDB in this study.

Water chemistry

Cations (Al^{3+}, Ca^{2+}, Fe, K^+, Li^+, Mg^{2+}, Mn, Na^+, and Si^{4+}) and anions (F^-, Cl^-, NO_3^-, PO_4^{2-}, and SO_4^{2-}) were analyzed using an inductively coupled plasma atomic emission spectrometer (PerkinElmer Co. model Optoma 7300DV) and an ion chromatograph (Dionex Co. model ICS2000), respectively, at the Cheonan Center of the Mine Reclamation Corporation (Seoul, Korea). Alkalinity was measured in the microbiology laboratory at Montana State University by an acidimetric titration of carbonate (Stumm and Morgan, 1996). The concentration of HCO_3^- and saturation indices (SI) of calcite in the hot spring waters were calculated using the program *Geochemist's Workbench*® (Bethke, 1996, 1998). Note that the measured alkalinity was used as carbonate alkalinity in the geochemical modeling calculations.

RESULTS

X-ray diffraction

The XRD patterns of the solid samples (precipitated mineral phases and associated microbial biomass) collected from areas L1–L4 showed several intense peaks that were assigned to calcite (Cal) (Figure 2). The *d* spacing with corresponding º2θ for calcite precipitate from area L4 was compared with the JCPDS reference (Table 1). Shifting of the peak at 29.88º2θ was evident. In addition, several weak peaks, assigned to aragonite (Ara), were detected in the samples collected from areas L2, L3, and L4. The relative weight percent of the two carbonate phases (calcite and aragonite) estimated from the integral intensities of calcite 012 and aragonite 111 in the pattern of L4 was ~89:11, according to the method described above.

Table 1. Comparison of XRD measurements of calcite (L4) with the JCPDS reference.

Measured, º2θ	23.18	29.88	31.51	36.16	39.56	43.36	47.50	48.65
(*d* spacing, Å)	(3.83)	(2.99)	(2.94)	(2.48)	(2.28)	(2.09)	(1.91)	(1.87)
JCPDS, º2θ	23.02	29.36	31.50	36.04	39.13	43.04	47.57	48.63
(*d* spacing, Å)	(3.86)	(3.04)	(2.84)	(2.49)	(2.30)	(2.10)	(1.91)	(1.87)

Stable isotopes

The carbon isotope compositions of the calcium carbonates collected from the four sampling locations in the study area are shown in Table 2. Note that the standard deviation of the reported $\delta^{13}C$ value in Table 2 presents the isotopic distribution of the sample itself given that the overall analytical precision for the $\delta^{13}C$ measurement is <0.04‰. All of the calcium carbonate samples were ^{13}C-enriched relative to the DIC of the water sample collected from the hot spring vent or the water source. Furthermore, the carbon isotope composition of the calcium carbonates ranged from +0.98‰ to +3.20‰, increasing with distance of the calcium carbonates from the hot spring vent.

Water chemistry

Concentrations of various cations and anions as well as other geochemical parameters, such as temperature, pH, and alkalinity of the hot spring waters from the four sampling areas (L1−L4), are summarized in Table 3. Regardless of the sampling site, all the spring waters had neutral pH values (6.7−7.2) and were enriched in Ca^{2+}, Mg^{2+}, Na^{+}, and SO_4^{2-} ions. In addition, alkalinity values determined from L1−L3 sampling sites were identical to each other except for that from L4. Saturation indices (SI) calculated on the basis of the geochemical data presented in Table 3 showed that the water from L4 (SI = 1.07) was more supersaturated with respect to calcite than those from L1 (SI = 0.63), L2 (SI = 0.74), and L3 (SI = 0.61).

Optical microscopy

Polarizing optical microscopy (POM) showed the distribution of organic matter (dark areas) and mineral phases (light granules) associated with the solids collected from the different areas of the spring (Figure 3). The dark areas in this case were identified as the OM associated with microbial biomass. The light granules (arrow in Figure 3a) associated with the suspended microbial mat from area L1 were ~50 μm across, arranged in irregularly shaped clusters and in intimate contact with the microbial biomass. Based on the XRD data, these granules are probably calcium carbonate grains. Samples from areas L2 and L3 contained similar, irregularly shaped clusters of grains. By contrast, the light granules (arrow in Figure 3b) in the sample from the mound at L4 were arranged in layers that were separated from each other by layers of filamentous microbial biomass. Such layered structures were not seen in the suspended microbial mats at areas L1−L3.

Table 2. Stable isotope data for calcium carbonates and dissolved inorganic carbon.

Sample	Number*	$\delta^{13}C_{carbonate}$ (‰)
Calcium carbonates		
L1	3	3.20 ± 0.40
L2	3	1.50 ± 0.37
L3	3	1.12 ± 0.07
L4	3	0.98 ± 0.02
DIC	5	−7.25 ± 0.42

DIC = dissolved inorganic carbon
* The number of individual analyses

Electron microscopy

Scanning electron microscopic examination of the solids collected from area L2 revealed calcified filaments 1−3 μm wide which resemble the morphology of non-calcified cyanobacterial filaments in other areas of the suspended biomass (Figure 4a). Other mineralized structures appeared as clusters of randomly distributed and parallel-aligned round plates surrounding a central void space (arrows in Figure 4b). The size of the voids ranged from sub-micron to 3 μm in diameter. Calcified 1−3 μm-diameter structures were often observed extending between clusters of plates (Figure 4b).

Examination by SEM of the solids from area L1 showed aggregates of sub- and anhedral-platy grains 2−3 μm in size as well as larger platy bodies with cylindrical void spaces (Figure 5a,c). The magnified image of the area outlined in Figure 5a shows the grains to consist of crystals with a rhombohedral face (Figure 5b). Larger grain structures 10−30 μm long and 4−10 μm wide were also observed on the magnified image of the area outlined of Figure 5c that appeared to

Table 3. Solution chemistry of La Duke hot spring, Yellowstone National Park.

Site	L1	L2	L3	L4
Temperature (ºC)	62	62	62	65
pH	6.7	6.7	6.7	7.2
Alkalinity (mg/L, $CaCO_3$)	300	300	300	280
Eh (mV)	500	500	500	500
Al^{3+}	N.D	N.D	N.D	N.D
Ca^{2+}	396.32	391.58	393.10	380.68
Fe	0.33	0.39	0.40	0.28
K^{+}	29.79	29.63	30.09	28.64
Li^{+}	0.40	0.41	0.41	0.39
Mg^{2+}	77.62	76.33	77.44	73.93
Mn	N.D	N.D	0.01	N.D
Na^{+}	211.16	206.79	223.86	201.37
H_4SiO_4	80.63	80.87	81.59	77.82
F^{-}	2.53	2.07	1.69	1.48
Cl^{-}	N.D	N.D	N.D	N.D
NO^{3-}	N.D	N.D	N.D	N.D
PO_4^{2-}	0.31	1.16	1.38	2.25
SO_4^{2-}	1295.52	563.21	1360.35	1320.31
*HCO_3^{-}	343.00	337.27	343.49	315.07

Units: mg/L, detection limits: <0.1 μg/L for most elements
* Denotes a calculated value for free HCO_3^{-} ions
N.D.: not detected

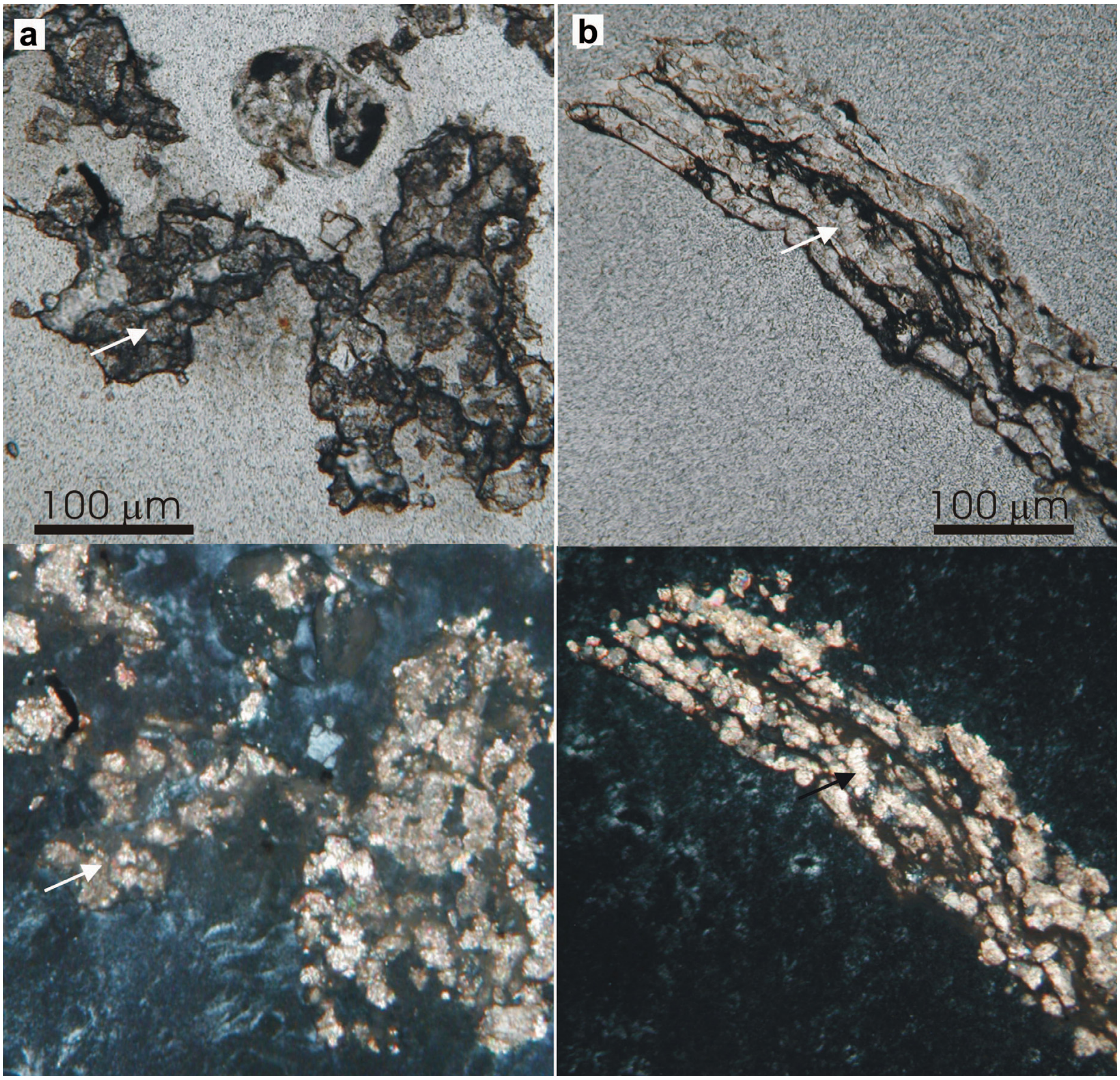

Figure 3. Optical photomicrographs of solid material collected from areas L1 (a, upper and lower) and L4 (b, upper and lower). The upper images were obtained in plane-polarized light, while the lower images were obtained with the polars crossed . The dark regions resolved with plane polars correspond to organic matter (microbial biomass) while the light regions resolved with crossed polars correspond to the mineral phase (calcium carbonate precipitates) as indicated by the arrows.

be cemented together by a fibrous matrix (arrow in Figure 5d). One of the larger grains in the sample from area L1 detected by SEM was composed of a series of parallel plates of decreasing size stacked on top of one another (Figure 6a). When this grain was sectioned by FIB and analyzed by TEM-EDS, variations in C, O, Ca, S, Fe, and Si abundance were observed in different regions of the grain, suggesting a heterogeneous composition (Figures 6b,c). Calcium is dominant in region 1 and Fe in region 3. Selected area electron diffraction (SAED) patterns corresponding to regions 1, 2, and 3 revealed different Bragg's reflection patterns (Figure 6d). The elemental composition, electron diffraction pattern, and extension of bend contour in region 1, referred to hereafter as the central region, indicate that it is composed of crystalline calcite (Figure 6, region 1). The diffuse halo patterns obtained from regions 2 and 3, referred to hereafter as peripheral regions, are consistent with an amorphous structure (Figure 6, regions 2 and 3). However, the abundance of Fe and the calculated Debye-Scherrer ring pattern (Yvon *et al.*, 1977) indicate the co-occurrence of a hematite phase in region 3. Solids from area L3 exhibited similar characteristics to those described above for solids from areas L1 and L2.

The mineral layer of the solid material recovered from area L4, when viewed by SEM, contained grains

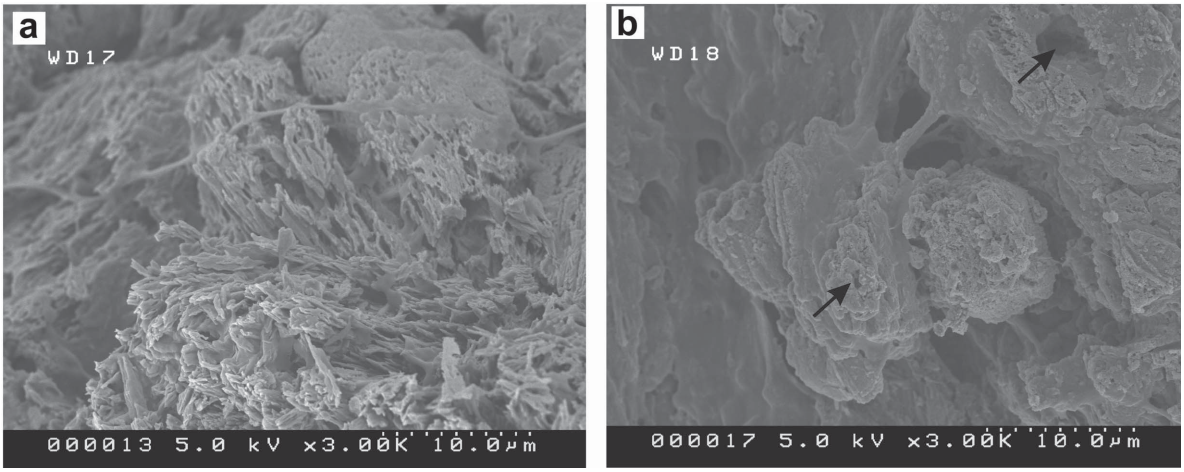

Figure 4. SEM images of a sample collected from area L2 displaying (a) calcified filaments 1−3 μm wide extending across or (b) between the calcium carbonate aggregates. Clusters of randomly distributed and parallel-aligned round plates surrounding a central void space were also observed (arrows).

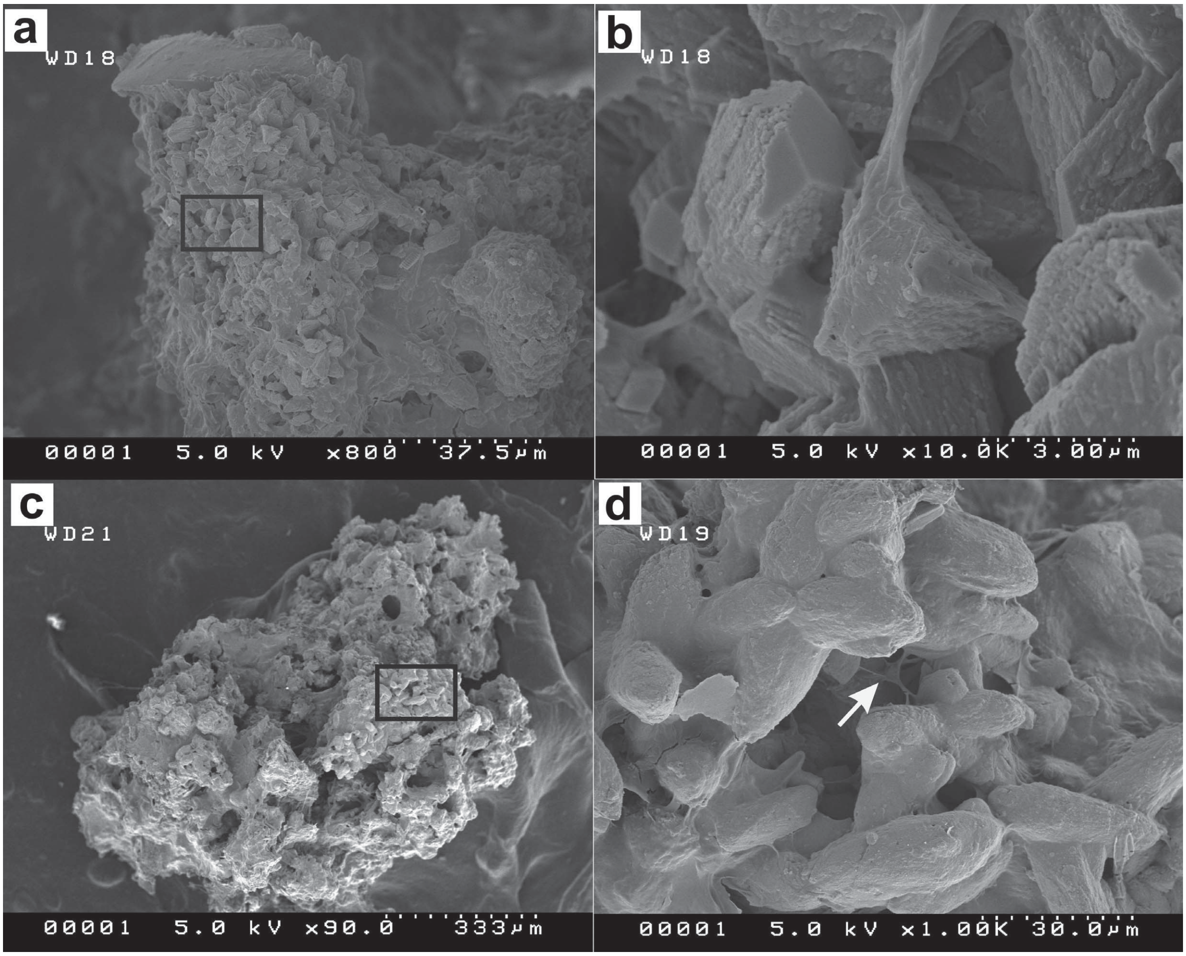

Figure 5. SEM images of a sample collected from area L1 displaying (a) the aggregates consisting of sub- and anhedral platy grains 2−3 μm wide and (c) of larger platy bodies with cylindrical void space. In magnified images, calcium carbonate clearly has precipitated with a rhombohedral face (b) and grains cemented with a fibrous matrix (arrow, d).

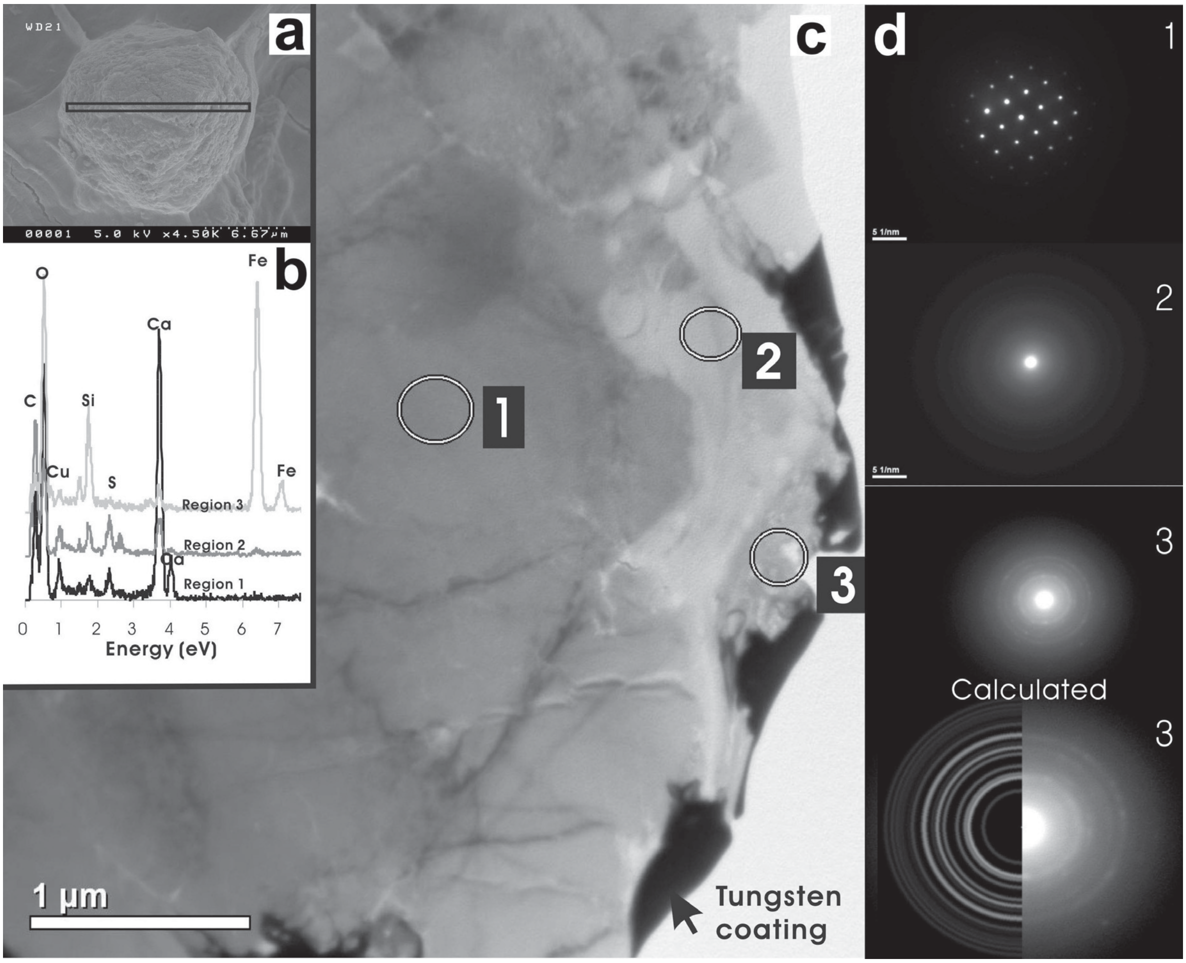

Figure 6. TEM image of the calcium carbonate grain in area L1 sectioned from the region marked on the SEM image (inset, a), by means of a FIB technique, displaying the inside central area (1) and two regions (2 and 3) in the periphery. The SAED pattern with EDS shows a crystalline calcite (region 1), the amorphous phase with Ca and Si (region 2) with the diffuse halo, and the hematite phase (region 3) along with the calculated Debye-Scherrer ring pattern.

with a morphology similar to those observed in samples collected from areas L1 and L2 (Figure 7). However, their profiles were generally obscured by a coating or film of material. When an unobscured grain (Figure 8a) was sectioned by FIB and analyzed by SAED-TEM, it contained central areas that produced diffraction patterns and bend contours consistent with the presence of monocrystalline calcite (Figure 8b,c). Regions at the periphery of a grain that yielded a diffraction pattern representative of calcite were often adjacent to or surrounded by regions containing amorphous material that produced no measurable diffraction pattern (Figure 8c, circled area). These regions generally contained voids, crystalline calcite (see the arrows), and amorphous material (see arrowhead) (Figure 8d). The periphery of a grain produced different EELS spectra from the central area (Figure 9a). At the periphery, the C-K edge at 288.5 eV indicated a poorly ordered carbon (OM)-based structure with a C:Ca:O ratio of 25:1:75.

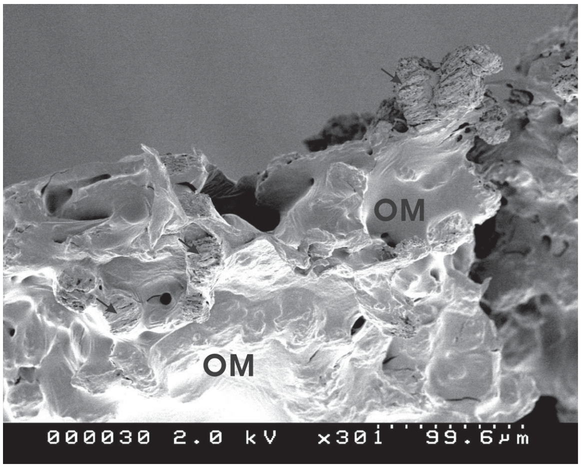

Figure 7. SEM image of sample collected from area L4 displaying accretions of porous fossilized filament (arrows) in the organic matter (OM) matrix.

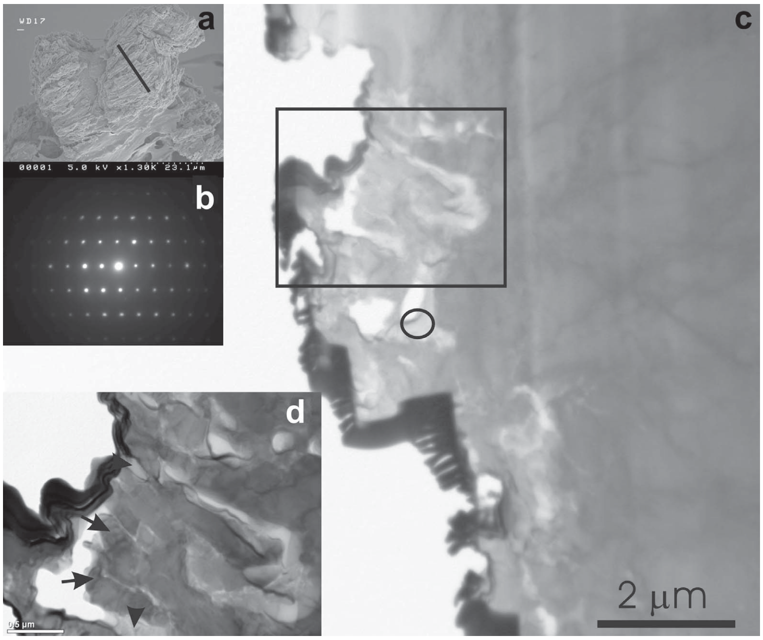

Figure 8. TEM image of the calcium carbonate grain in area L4, sectioned from the area marked on the SEM image (a) showing a dense central area and the porous structure existing near the periphery only, in a cross-sectional view. The SAED pattern for the dense central region showed typical Bragg's reflections of crystalline calcite. Measurable diffractions were not detected from the porous periphery (circled area) indicating an amorphous phase. The inset, magnified TEM image (d) of the area outlined shows (arrows) calcite crystals infilling the amorphous material (arrowhead) surrounding the growing calcite blocks in the pore area.

Furthermore, the periphery did not produce the strong carbonate ion peak (Car) at 290 eV and Ca L_{23} peak at ~346 eV with a C:Ca:O ratio of 27:23:50 that was detected in the central region of the grain. The SAED

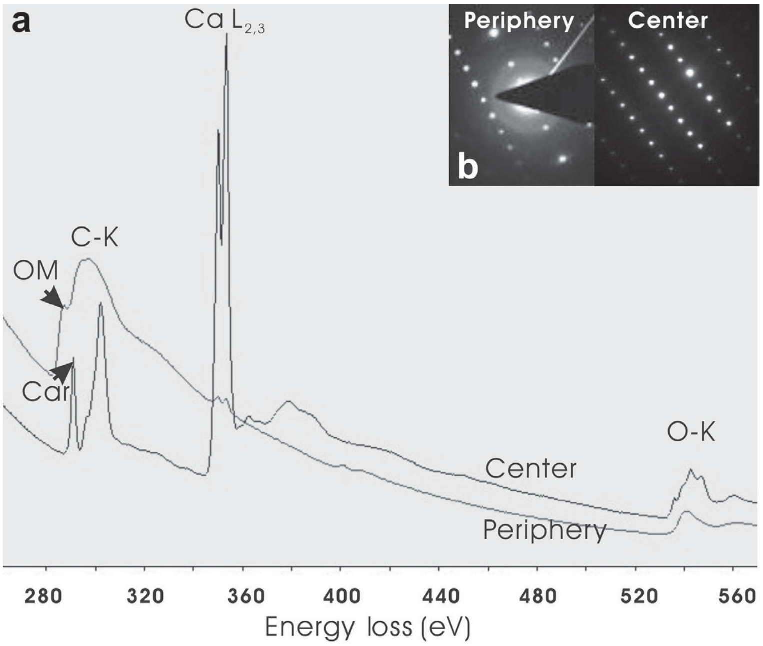

Figure 9. EELS spectra for the porous periphery and solid central region of the grain from area L4. The diagnostic organic matter (OM) peak at 288.5 eV was detected in the periphery, whereas the strong intensity of carbonate ion at 290 eV and Ca L_{23} at ~346 eV were detected in the central region (a). The corresponding SAED pattern showed a mixture of crystalline calcite and amorphous phase for the periphery and crystalline calcite phase for the central region (b).

patterns suggested a mixture of crystalline and amorphous calcite at the periphery and a discrete crystalline calcite phase in the central area (Figure 9b).

DISCUSSION

Isotopic signature of calcium carbonate precipitates

The carbon isotope composition of the laminated carbonate minerals closest to the source was most similar to that of DIC in water emanating from the source. This observation, along with the highest pH value determined from L4, supports the idea that abiogenic processes, such as rapid CO_2 degassing, were more dominant in the formation of the calcium carbonates collected from L4 (Fouke *et al.*, 2000). For example, the lighter carbon isotope (^{12}C) has been shown to be preferentially removed from the DIC pool during a biological process, such as photosynthetically driven carbon fixation into OM by cyanobacteria, thus resulting in a ^{12}C-depleted or ^{13}C-enriched DIC pool (Cummings and McCarty, 1982; McConaughey, 1989; Guo *et al.*, 1996). Therefore, the enrichment of ^{13}C in the calcium carbonate minerals (L1) formed along with suspended microbial biomass suggests that the DIC pool had become ^{13}C-enriched due to microbial activities in this environment (L1) prior to the calcium carbonate precipitation. Furthermore, the systematic increase in $\delta^{13}C$ of the calcium carbonates as a function of distance from the spring source suggests a different degree of biological or photosynthetic activities across the sampling sites.

Structure of calcium carbonate precipitates

The laminar structure (Figures 3b, 7) in area L4, consisting of multilayers of biomass and calcified filament which developed into the mound immediately downstream from the spring source, was formed primarily as a result of rapid degassing of CO_2 from the source water. The calcified filament in laminae reflects episodic microbial involvement in calcite deposition (Guo *et al.*, 1996). The aggregated structure observed in a stagnant pool is probably due to a different topography condition compared with the laminae on the mound where the water flows and evaporates rapidly. Based on the data from the present study, the formation of calcium carbonate near the source is suggested to proceed as follows: (1) association of dissolved carbonate and calcium ions with microbial biomass; (2) precipitation of calcium carbonate in the vicinity of microbial biomass; (3) formation of dendritic void space; and (4) void infilling by further calcium carbonate precipitation. High-magnification TEM results of the present study suggest that infilling of the voids proceeds from the porous periphery of the grain inward. These void-filling calcium carbonates observed in the samples from L4 are thought to be of abiotic origin associated with the rapid CO_2 degassing described earlier. Under the highest supersaturation (SI = 1.07) with respect to calcite among the sampling sites tested in this study, abiotic processes must have been dominant (Ford and Pedley, 1996; Jacobson and Usdowski, 1975) in L4 over the course of formation of the calcium carbonate. In addition, CO_2 degassing would have been much more effective and intense in L4, as shown by the highest solution pH, because of its unique topographical feature (see Figure 1). The $\delta^{13}C$ value of the calcium carbonates collected from L4 was closer to that of the DIC in the study area than that of the carbonates collected from L1, suggesting dominant abiotic calcium carbonate precipitation in L4. Recent studies have suggested, however, that photosynthesis remains an important process for calcium carbonate precipitation in many natural settings, including highly carbonate-supersaturated systems (Shiraishi *et al.*, 2008, 2010). No evidence of formation of Mg-rich carbonates was detected by XRD or TEM-EDS, probably due to the low Mg:Ca ratios of ~0.2 in water, regardless of sampling locations.

The periphery of a calcite grain close to the source. The amorphous nature of the periphery of a calcite grain appeared to consist of a mixture of calcium carbonate and organic material (OM). As shown in Figure 9, the low intensity of the Ca L_{23} peak and no measureable carbonate peak in EELS indicated the mixture of OM and absorbed Ca element to OM (Benzerara *et al.*, 2005; Aloisi *et al.*, 2006). The formation of ACC was reported in the nucleation stage of calcium carbonate mineral formation (Aloisi *et al.*, 2006; Obst *et al.*, 2009a) or during mineral growth when controlled biologically (Weiss *et al.*, 2002; Baronnet *et al.*, 2008). In the present study, ACC seems not to have been formed, however, because the amorphous phase detected in the SAED pattern was attributed to organic material. Thus, a calcium carbonate mineral, formed by rapid CO_2 degassing from the source water grows by continuous extension of a single crystal of calcite, incorporating freshly precipitated mineral into the core crystalline structure through a void-infilling process. The presence of traces of sulfur in the EDS spectra further suggests that other elements present as dissolved ions (Table 3) in the source water were incorporated into the calcite structure during the crystal growth. Furthermore, the occurrence of Fe (oxyhydr)oxide or silica near the voids suggest that they co-precipitate from solution along with the calcium carbonate. The partial substitution of calcium by Mg or Fe in calcite structure results in a peak shift in XRD measurement, and the appearance of *c* reflections along [104] in the SAED pattern according to Reksten (1990). In the XRD profiles, the main peak of calcite at 29.36°2θ was clearly shifted to 29.88°2θ, indicating the structural modification. In the present study, the *c* reflections from the sample L4 (not shown) were also detected in the SAED pattern. Further study of the crystallographic modeling of calcite structure should be performed to understand the unpredicted characteristics in calcite structure associated with sulfur content as an impurity.

The periphery of a calcite grain with distance from the source. Whereas the periphery of a calcite grain close to the source displayed a mixture of crystalline calcite and amorphous material in void areas (Figure 8d), no evidence of this was observed for calcite grains found distant from the source (Figure 6c), indicating the different precipitation processes at different locations. The similar structure of the irregular aggregates composed of micron-sized granules with biomass that formed subglobular bodies in the pool more distant from the source (Figures 3a, 5) was also observed in other hot springs (Chafetz and Folk, 1984; Folk *et al.*, 1985; Casanova, 1986) where the abundance of cyanobacteria increases downstream (Guo *et al.*, 1996; Whitton and Potts, 2000), causing the relatively long-term photosynthetic activity, continuously removing ^{12}C, and thus precipitating ^{13}C-enriched calcium carbonates in the stagnant pool. The microbial consortia probably change away from the source due to changes in nutrients. The discernible void infilling of calcium carbonate precipitation seems not to be the case in the pool where the biotic processes result in ^{13}C-enriched DIC and subsequently yielded calcium carbonate precipitation with a larger δ^{13}C value than the other location of the calcium carbonates near the source.

CONCLUSIONS

Depending on the sampling locations where abiotic CO_2 degassing or a biotic reaction is more dominant during the formation of calcium carbonate minerals, the structure of the cross-sectional view of the calcite grain examined by the combination of TEM and EELS at nano-scale seemed to be different. The calcite void infilling in porous OM-rich areas of the periphery was observed only near the source where the CO_2 is extremely degassed and the water is most supersaturated with respect to calcite. The systematic variations in the δ^{13}C value and the saturation indices of calcium carbonates in the spring water at different locations support the increased biological activities across the sampling sites in the study area.

ACKNOWLEDGMENTS

This research was supported by the Basic Science Research Program through the National Research Foundation of Korea (NRF) funded by the Ministry of Education, Science and Technology (20110013407) to Jin-wook Kim, and the Joint Research Project under the Korea-Japan Basic Scientific Cooperation Program through the Japan Society for the Promotion of Science (JSPS) to Toshihiro Kogure (09032211-000486). S.-T. Kim acknowledges financial support from the NSERC Discovery Grants Program. This work was partially supported (Young-Nam Jang) by the 'Utilization and Sequestration of CO_2 by using industrial minerals' program. The authors are grateful to E. Fujii at the University of Tokyo for preparing the TEM specimen by means of FIB.

REFERENCES

Atekwana, E.A., Atekwana, E., Legall, F.D., and Krishnamurthy, R.V. (2004) Field evidence for geophysical detection of subsurface zones of enhanced microbial activity. *Geophysical Research Letters*, **31**, 1–5.

Aloisi, G. (2008) The calcium carbonate saturation state in cyanobacterial mats throughout Earth's history. *Geochimica et Cosmochimica Acta*, **72**, 6037–6060.

Aloisi, G., Gloter, A., Krüger, M., Wallmann, K., Guyot, F., and Zuddas, P. (2006) Nucleation of calcium carbonate on bacterial nanoglobules. *Geology Society of America*, **34**, 1017–1020.

Arp, G., Reimer, A., and Reitner, J. (2001) Photosynthesis-induced biofilm calcification and calcium concentrations in Phanerozoic Oceans. *Science*, **292**, 1701–1704.

Baronnet, A., Cuif, J.P., Dauphin, Y., Farre, B., and Nouet, J. (2008) Crystallization of biogenic Ca-carbonate within organo-mineral micro-domains. Structure of the calcite prisms of the Pelecypod *Pinctada margaritifera* (Mollusca) at the submicron to nanometre ranges. *Mineralogical Magazine*, **72**, 617–626.

Benzerara, K., Yoon, T.H., Menguy N., Tyliszczak, T., and Brown Jr., G.E. (2005) Nanoscale environments associated with bioweathering of a Mg-Fe-pyroxene. *The National Academy of Sciences*, **102**, 979–982.

Bethke, C.M. (1996) *Geochemical Reaction Modeling: Concept and Applications*. Oxford University Press, New York.

Bethke, C.M. (1998) *The Geochemist's Workbench, Version 3.0: A Users Guide to Rxn, Act2, Tact, React, and Gtplot*. Hydrogeology Program, University of Illinois, Urbana, Illinois, USA.

Bosak, T. and Newman, D.K. (2003) Microbial nucleation of calcium carbonate in the Precambrian. *Geology*, **31**, 577–580.

Casanova, J. (1986) East African rift stromatolites. Pp. 201–210 in: *Sedimentation in the African Rifts* (I.E. Frostick, R.W. Renaut, I. Reid, and J.J. Tiercelin, editors). Special Publication, **25**. Geological Society of London.

Castanier, S., Métayer-Levrel, G.L., and Perthuisot, J.P. (1999) Ca-carbonates precipitation and limestone genesis – the microbiogeologist point of view. *Sedimentary Geology*, **126**, 9–23.

Chafetz, H.S. and Folk, R.L. (1984) Travertines: depositional morphology and the bacterially constructed constituents. *Journal of Sedimentary Petrology*, **54**, 289–316.

Cummings, C.E. and McCarthy, H.M. (1982) Stable carbon isotope ratios in Astrangia danae: evidence for algal modification of carbon pools used in calcification. *Geochimica et Cosmochimica Acta*, **6**, 1125–1129.

Dittrich, M., Muller, B., Mavrocordatos, D., and Wehrli, B. (2003) Induced calcite precipitation by cyanobacterium Synechococcus. *Acta Hydrochimica et Hydrobiologica*, **31**, 162–169.

Folk, R.L., Chafetz, H.S., and Tiezzi, P.A. (1985) Bizarre forms of depositional and diagenetic calcite in hot spring travertines, central Italy. Pp. 349–369 in: *Carbonate Cements* (N. Schneidermann and P. Harris, editors). SEPM Special Publication, **36**, Society for Sedimentary Geology, Tulsa, Oklahoma, USA.

Ford, T.D. and Pedley, H.M. (1996) A review of tufa and travertine deposits of the world. *Earth-Science Reviews*, **41**, 117–175.

Fouke, B.W. , Farmer, J.D., Marais, D.J.D., Pratt, L., Sturchio, N.C., Burns, P.C., and Discipulo, M.K. (2000) Depositional facies and aqueous-solid geochemistry of travertine-depositing hot springs (Angel Terrace, Mammoth Hot Springs, Yellowstone National Park, U.S.A.). *Journal of Sedimentary Research*, **70**, 565–585.

Fouke, B.W., Bonheyo, G.T., Sanzenbacher, B., and Frias-Lopez, J. (2003) Partitioning of bacterial communities between travertine depositional facies at Mammoth Hot Springs, Yellowstone National Park, U.S.A. *Canadian Journal of Earth Sciences*, **40**, 1531–1548.

Guo, L., Andrews, J., Riding, R., Dennis, P., and Dresser, Q. (1996) Possible microbial effects on stable carbon isotopes in hot-spring travertines. *Journal of Sedimentary Research*, **66**, 468–473.

Jacobson, R.L. and Usdowski, E. (1975) Geochemical controls on a calcite precipitating spring. *Contributions to Mineralogy and Petrology*, **51**, 65–74.

Kameda, J., Saruwatari, K., Beaufort, D., and Kogure, T. (2008) Textures and polytypes in vermiform kaolins diagenetically formed in a sandstone reservoir: a FIB-TEM investigation. *European Journal of Mineralogy*, **20**, 199–204.

Kandianis, M.T., Fouke, B.W., Johnson, R.W., Veysey, J., and Inskeep, W.P. (2008) Microbial biomass: A catalyst for CaCO$_3$ precipitation in advection-dominated transport regimes. *Geological Society of America Bulletin*, **120**, 442–450.

Kim, J.W. and Dong, H. (2011) Application of electron energy-loss spectroscopy (EELS) and energy-filtered transmission electron microscopy (EFTEM) to the study of mineral transformation associated with microbial Fe-reduction of magnetite. *Clays and Clay Minerals*, **59**, 176–188.

Knorre, H.V. and Krumbein, W.E. (2000) Bacterial calcification. Pp. 25–31 in: *Microbial Sediments* (R.E. Riding and S.M. Awramik, editors). Springer, Berlin.

Kogure, T. (2003) A program to assist Kikuchi pattern analysis. *Journal of the Crystallographic Society of Japan*, **45**, 391–395.

McConaughey, T. (1989) ^{13}C and ^{18}O isotopic disequilibrium in biological carbonates: I. patterns. *Geochimica et Cosmochimica Acta*, **53**, 151–162.

McCrea, J.M. (1950) On the isotopic chemistry of carbonates and a paleotemperature scale. *The Journal of Chemical Physics*, **18**, 849–857.

Merz-preiβ, M. (2000) Calcification in cyanobacteria. Pp. 50–56 in: *Microbial Sediments* (R.E. Riding and S.M. Awramik, editors). Springer, Berlin.

Merz-Preiβ, M. and Riding, R. (1999) Cyanobacterial tufa calcification in two freshwater streams: ambient environment, chemical thresholds and biological processes. *Sedimentary Geology*, **126**, 103–124.

Obst, M., Wehrli, B., and Dittrich, M. (2009a) CaCO$_3$ nucleation by cyanobacteria: laboratory evidence for a passive, surface-induced mechanism. *Geobiology*, **7**, 324–347.

Obst, M., Dynes, J.J., Lawrence, J.R., Swerhone, G.D.W., Benzerara, K., Karunakaran, C., Kaznatcheev, K., Tyliszczak, T., and Hitchcock, A.P. (2009b) Precipitation of amorphous CaCO$_3$ (aragonite-like) by cyanobacteria: A STXM study of the influence of EPS on the nucleation process. *Geochimica et Cosmochimica Acta*, **73**, 4180–4198.

Pentecost, A. (1985) Association of cyanobacteria with tufa deposits: identity, enumeration and nature of the sheath material revealed by histochemistry. *Geomicrobiology Journal*, **4**, 285–298.

Pentecost, A. (2003) Cyanobacteria associated with hot spring travertines. *Canadian Journal of Earth Sciences*, **40**, 1447–1457.

Pentecost, A. and Riding, R. (1986) Calcification in cyanobacteria. Pp. 73–90 in: *Biomineralization in Lower Plants and Animals* (B.S.C. Leadbeater and R. Riding, editors). Special Publication, **30**, Systematics Association, UK.

Pratt, B.R. (2001) Calcification of cyanobacterial filaments: Girvanella and the origin of lower Paleozoic lime mud. *Geological Society of America*, **29**, 763–766.

Reksten, K. (1990) Superstructures in calcite. *American Mineralogist*, **75**, 807–812.

Robbins, L.L. and Yates, K.K. (1998) Production of carbonate sediments by a unicellular green alga. *American Mineralogist*, **83**, 1503–1509.

Schultze-Lam, S., Fortina, D., Davisa, B.S., and Beveridge, T.J. (1996) Mineralization of bacterial surfaces. *Chemical Geology*, **132**, 171–181.

Shiraishi, F., Reimer, A., Bissett, A., Beer, D., and Arp, G. (2008) Microbial effects on biofilm calcification, ambient water chemistry and stable isotope records in a highly supersaturated setting (Westerhöfer Bach, Germany). *Palaeogeography, Palaeoclimatology, Palaeoecology*, **262**, 91–106.

Shiraishi, F., Okumura, T., Takahashib, Y., and Kanoa, A. (2010) Influence of microbial photosynthesis on tufa stromatolite formation and ambient water chemistry, SW Japan. *Geochimica et Cosmochimica Acta*, **74**, 5289–5304.

Stumm, W. and Morgan, J.J. (1996*) Aquatic Chemistry*: *Chemical Equilibria and Rates in Natural Waters.* John Wiley and Sons, New York.

Thompson, J.B. and Ferris, F.G. (1990) Cyanobacterial precipitation of gypsum, calcite, and magnesite from natural alkaline lake water. *American Mineralogist*, **18**, 995–998.

Weiss, I.M., Tuross, N., Addadi, L., and Weiner, S. (2002) Mollusc larval shell formation: amorphous calcium carbonate is a precursor phase for aragonite. *Journal of Experimental Zoology*, **293**, 478–491.

Weisse, D.J., Cretzmeyer, J.W., Crespi, A.M., Howard, W.G., and Skarstad, P.M. (1993) Electrochemical cells with end-of-service indicator. *United States patent*, H01M 614

Whitton, B. A. and Potts, M. (2000) The Ecology of Cyanobacteria: their Diversity in Time and Space. Kluwer Academic Publishers, Dordrecht, The Netherlands, 669 pp.

Yvon, K., Jeitschko, W., and Parthe, E. (1977) LAZY PULVERIX, a computer program, for calculating X-ray and neutron diffraction power patterns. *Journal of Applied Crystallography*, **10**, 73–74.

(*Received 16 February 2012; revised 18 October 2012; Ms. 654; AE: M. Kawano*)